Toward Absolute Phase Change Recovery With InSAR: Correcting for Earth Tides and Phase Unwrapping Ambiguities

Xiaohua Xu and David T. Sandwell

***Abstract*— Radar interferograms provide a map of the phase difference between the reference and repeat acquisitions modulo 2π. Under ideal conditions, the phase can be unwrapped to provide an absolute phase connection across the map, although there is always an unknown integer phase ambiguity (i.e., $N2\pi$) for the entire map. Here, we demonstrate a practical time series method to solve for these integer ambiguities in order to recover the absolute phase change between the first and last SAR images. An important first step is to correct the phase of each SAR image for the well-known solid earth tide, which typically produces a line of sight offset ±150 mm, as well as, trends along and across each image of ∼20 mm. This tide correction significantly reduces the noise in the InSAR time series, especially at the L-band. These tidally corrected interferograms are then unwrapped and used to solve for a set of integer ambiguities that achieves phase closure when summing around loops in the stack. There is an infinite number of ambiguity combinations that achieve loop closure; thus, regularization is required. In contrast to previous studies that use a least-squares approach to find the ambiguities, we adopt an L_1-norm approach to find the minimum number of ambiguity corrections needed to achieve loop closure. We note that the split-spectrum ionospheric correction can introduce $N\pi$ ambiguities and suggest two approaches for correcting both $N2\pi$ and $N\pi$ ambiguities.**

***Index Terms*— Phase unwrapping ambiguities, signal aliasing, solid earth tide, time series analysis.**

I. Introduction

OVER the past several years, the Interferometric Synthetic Aperture Radar (InSAR) method has been transformed from a research tool for investigating 10s to 100s of SAR images to a research production tool for processing 1000s and 10 000s of images. This transformation was largely driven by the Sentinel-1A and 1B satellites, which are designed for InSAR time series. Four attributes of Sentinel-1 have enabled this transformation: 1) the satellite orbits are maintained within a 200-m tube which nearly eliminates baseline decorrelation, 2) the orbit accuracies are better than 30 mm in the radial direction and better than 70 mm in the along-track direction, which enables pure geometric coregistration of images [1], [2] (discussed below), and 3) the 250-km interferometric wide-swath mode enables complete coverage of tectonically active areas at a cadence of 12 days, with the possibility of 6-day full coverage in the case of a deformation event, and 4) most importantly, the data are completely free and open [3].

An important advantage of pure geometric coregistration of all the slave images to a single master is that it ensures phase closure among all interferograms in the stack [4]. It is clear that the sum of the interferometric phase around a loop consisting of three unfiltered interferograms is zero. Filtering interferograms result in some misclosure in decorrelated areas [5], but the global misclosure errors are always much smaller than the ambiguity phase of $N2\pi$ discussed in this article. The implication is that it is possible to establish an absolute phase connection between the first and last SAR image in a time series if the $N2\pi$ integer ambiguities can be resolved.

Suppose the ambiguities can be resolved for a large set of interferograms; then, for each pixel, the range versus time could be established using, for example, a Small Baseline Subset (SBAS) approach [6], [7]. With no smoothing, one would expect that the accumulated range would be equal to the surface deformation contaminated by the traditional error components associated with all geodetic measurements including, orbital error, atmospheric and ionospheric delay, solid earth tides and ocean loading tides. The largest errors are associated with the atmosphere and ionosphere, and there are many approaches to correcting or mitigating these errors [8]–[13]. Here, we first focus on the solid earth tide, which is known to an accuracy of better than 1 mm [14], and thus, can be eliminated from the error budget. The ocean loading tide is less well known but also largely correctable [15]–[17]. We then discuss a new type of ambiguity that can be introduced from the split-spectrum ionosphere correction. Finally, we discuss the overall approaches to ambiguity resolution.

II. Effects of Solid Earth Tide on SBAS Time Series

Previous studies suggested that the solid earth tide is not a significant error source for radar interferometry because it is largely a constant over distances of 100 km (i.e., typical of the

Manuscript received May 26, 2019; revised July 19, 2019; accepted September 5, 2019. Date of publication September 26, 2019; date of current version December 27, 2019. This work was supported by the NASA Earth Surface and Interior Program under Grant NNX16AK93G, in part by the National Science Foundation under Grant OAC-1834807, and in part by the Southern California Earthquake Center (SCEC) (18134) under the NSF Cooperative Agreement EAR-1033462 and USGS Cooperative Agreement G12AC20038. *(Corresponding author: Xiaohua Xu.)*

The authors are with the Institute of Geophysics and Planetary Physics, Scripps Institution of Oceanography, University of California San Diego, La Jolla, CA 92093 USA (e-mail: sddyxxh@gmail.com).

This article has supplementary downloadable material available at http://ieeexplore.ieee.org, provided by the authors.

Color versions of one or more of the figures in this article are available online at http://ieeexplore.ieee.org.

Digital Object Identifier 10.1109/TGRS.2019.2940207

TABLE I
TIDAL ALIASES FOR InSAR SATELLITE SAMPLING

	repeat days	M2	S2	K1	O1	P1
amplitude (mm)		384.83	179.05	191.78	158.11	70.88
ERS/Envisat	35	94.50	-	365.23	75.06	365.23
RADARSAT	24	64.07	-	365.23	77.70	365.23
ALOS-1	46	398.63	-	365.23	190.60	365.23
ALOS-2	14	270.08	-	365.23	1036.73	365.23
Sentinel-1A/B	12	64.07	-	365.23	77.04	365.23
NISAR	12	64.07	-	365.23	77.04	365.23
Sentinel-1A&B	6	14.77	-	365.23	14.19	365.23

previous generation of SAR satellites) [16]. However, there are two important enhancements provided by the new generation of SAR satellites, regular cadence with short baselines and swath widths and lengths of 250 km or greater. Here, we show how the solid earth tide contaminates InSAR time series and show that it can be easily corrected.

A. Tidal Aliasing

Unlike atmospheric or ionospheric contamination, which is largely random in time, the sun-synchronous orbits of the current generation of SAR satellites cause the diurnal and semidiurnal tides to be aliased into much longer periods. For example, the semidiurnal solar tide S2 has a period of one day and an amplitude of 180 mm (Table I). This tide component is aliased into zero frequency when sampled at an exact integer number of days. In general, the alias frequency f_a due to sampling a tide of frequency f_t at a frequency f_s is given by the following formula:

$$f_a = f_t - f_s \text{round}(f_t/f_s).$$

For example, the M2 tide, with a period of 0.517542 days, when sampled at an interval of 12 days, has an alias period of 64.07 days (Table I). The next largest tidal component K1 has an alias period of 365.23 days when sampled at an integer number of days. The overall result is the 12-day sampled tide has alias periods of 64.07, 365.23, and 77.04 days (Table I). The aliases at 64 and 77 days could be smoothed out with smoothness in an SBAS analysis. However, the aliases having a 1-year period could be confused with real deformation signals associated with seasonal variations in water loading [18], [19]. So, we need to understand how these tide signals contaminate InSAR time series.

B. Contamination of InSAR Time Series by Solid Earth Tide

To illustrate the effects of the solid earth tide on InSAR time series, we decompose the tide change between the reference and repeat images into three components, as shown in Fig. 1.

1) The first component [Fig. 1(a)] is a spatially uniform range change. Below, we discuss how this uniform component introduces noise into an InSAR time series.
2) The second component is due to the variation in incidence angle across the scene [Fig. 1(b)]. This results in a phase ramp in the range direction because of the variations in look angle with range.
3) The third component [Fig. 1(c)] is due to the spatial variations in tidal height within the scene mostly associated with very long InSAR swaths. We call the first component, the absolute tide, and the combined second and third components, the relative tide.

C. Absolute Tide

To investigate the adverse effects of the absolute value [Fig. 1(a)] of the solid earth tide on InSAR time series from Sentinel-1 at (C-band) and the future NISAR at (L-band), first, we sample the tidal signal at the cadence of Sentinel-1 and NISAR, and analyze that signal using a standard InSAR time series analysis to recover the amplitude and period of the noise. Fig. 2 (left) shows the solid earth tide at Los Angeles, CA, as sampled by the 12-day exact repeat orbits of Sentinel-1 and NISAR for a 3-year time interval. As discussed above, the sampled tide has alias periods of 64.07, 365.23, and 77.04 days (Table I). Also shown is the wrapped tide, which is the only part of the signal that is available in a single-look complex (SLC) image because phase is modulo 2π. The wrapped tide adds noise to the time series. Note that the amplitude of the wrapped tide is larger for L-band than C-band so the tidal contamination will also be larger.

Next, we form all possible, wrapped interferograms within a 60-day moving window and add a linear trend to represent a real tectonic signal. Finally, we use these redundant interferograms in an SBAS analysis with moderate smoothing to recover the time series that is contaminated by the tide. The results are shown in Fig. 2 (right). Tidal contamination is fairly small at C-band (∼10-mm maximum and 1.03-mm rms) and significantly larger at L-band (∼60-mm maximum and 19.9-mm rms) in this specific case. Fortunately, the solid earth tide is known to have an accuracy of better than 1 mm [14], so after tidal correction, these errors in the SBAS time series will be very small.

D. Relative Tide

The previous analysis is based on a uniform value for the tide over the SAR scene. However, with the large frames being provided by Sentinel-1 and NISAR, there is a trend in the tide that varies both along with range and azimuth. The trend in the range is mostly due to the change in look angle

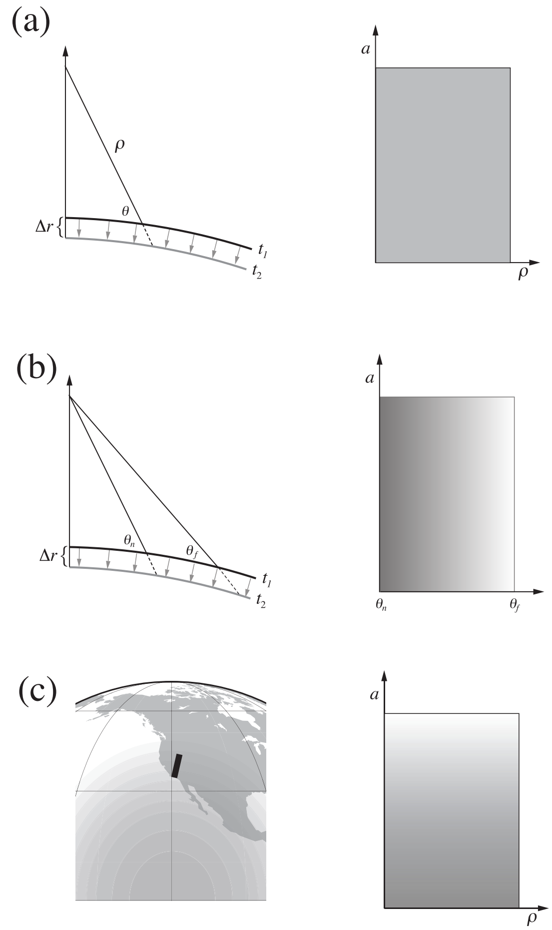

Fig. 1. (a) For a uniform incidence angle of θ, the radial component of the tide, projected into the line of sight of the radar, causes a uniform range change. Only the modulus of 1/2 of the radar wavelength λ remains in the interferogram to affect the time series since Δr is usually larger than λ. (b) Radial component of the tide maps into the LOS depending on the secant of the look angle. (c) Spatial variations in tide map directly into spatial variations in range. This is primarily a phase ramp in azimuth for mid-latitude regions.

across the swath. For a maximum tide amplitude of 180 mm, the LOS component will be 156 mm in the near range (29°) and 124 mm in the far range (46°) resulting in a 32-mm trend across the interferogram in range (Fig. 3). The tilt in azimuth depends on the change in latitude within a scene. As an example, the trend between Long Beach, CA, and Death Valley, CA (~300-km N-S distance) has a peak-to-trough amplitude of ~20 mm with the same sampling, as the Los Angeles tide. These trends in tide in both the range and latitude directions will go directly into the unwrapped interferogram so the effects will be identical at C-band and L-band (Fig. 3 shows tide error in mm with 10-mm contours). Again, we have generated synthetic interferograms from the 12-day sampling with a 60-day window and computed an SBAS time series with and without the tidal correction (Fig. 3). The results show an error curve having an amplitude of ~60 mm and a period of about 1 year with sub-oscillations of ~64/77 days. Without this correction, one could interpret the annual oscillation as a true annual signal when, in fact, it is the tidal signal aliased by the 12-day, sun-synchronous orbit of the SAR satellites.

III. Identifying and Correcting Integer Phase Ambiguities

A. Inversion Approach

An important step in the Global Navigation Satellite System (GNSS) data processing is to measure the integer number of wavelengths between the satellites and the receiver to provide an absolute position. Errors in this integer count are called integer phase ambiguities or cycle slips, and there is a large body of literature devoted to resolving integer phase ambiguities [20], [21]. Interferograms are inherently phased difference measurements between a reference and repeat image. One example is the geocoded SLC [22], which is an attempt to correct the phase of each SAR image to a common topographic surface and the correction applies an integer and fractional phase shift between the radar pixel and a matching point on the ground. Nevertheless, interferograms made from these SLCs have 2π integer ambiguities after the phase is unwrapped. If not properly corrected, this ambiguity term will affect every pixel in radar acquisitions and introduce a random walk type error that will bias the time series (Fig. 4). One way to partially correct InSAR time series for this phase unwrapping ambiguity is to set the displacement of some small patch of each map in the stack to zero, thus solving for the displacement time series of all other points relative to that stable location [7]. One problem with this approach is that atmospheric errors in that small patch will impose a phase shift over that entire interferogram, thus introducing phase noise to the resulting InSAR time series. Also, by forcing the patch to zero in a time-series, the resulting velocity uncertainties for that small area will be significantly underestimated. Of course, one could adjust each interferogram to match the line-of-sight deformation observed by continuous GNSS receivers in the scene [23]. However, this type of correction is dependent on the GNSS station density, which is not ideal for all situations.

Several examples of SBAS inversions, when a small number of interferograms have $N2\pi$ integer ambiguities, are provided in Fig. 4. The first case [Fig. 4(a) and (b)] illustrates the effects of two misclosure errors on an SBAS solution for a displacement time series. When the minimum set of 12-day interferograms are used, the displacement time series will have jumps at times between the two ambiguities. Keeping just two ambiguities but adding more interferograms in a 24-day window results in smaller steps in the displacement time series. When the window is increased to 36 days, the steps are much smaller. However, this is an unrealistic case because the number of ambiguities will increase with the number of interferograms. A more realistic case is provided in Fig. 4 (g) and (h) where the window is increased to 60 days, and 30% of the interferograms have both positive and negative ambiguities. The input signal consists of a trend plus an annual cycle and some atmospheric noise. When no unwrapping ambiguity exists in the interferograms, the recovered signal (magenta), given certain smoothness, lies within the atmospheric noise envelope. The resulting SBAS time-series (green), with the adverse effect from the ambiguities, drifts more than 20 mm from the input signal.

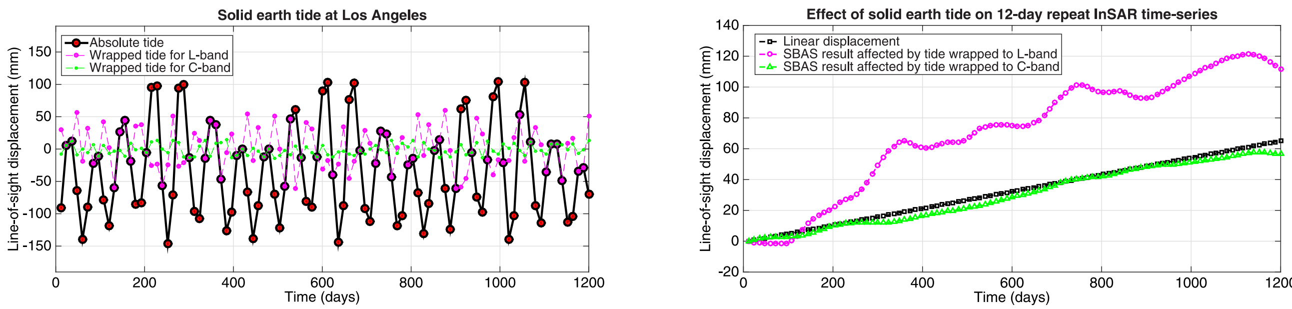

Fig. 2. (Left) Line-of-sight component of the solid earth tide at Los Angeles, California (118.2° W, 33.75° E) when sampled at 12 days by Sentinel-1 and NISAR. This sampling results in aliased components at 64.07, +/−365.23, and 70.04 days. Also shown is the tide wrapped for C-band and L-band as an indication of the noise contribution to interferometry. (Right) Synthetic InSAR time series consisting of a linear displacement versus time (black) and the recovered displacement versus time when the wrapped solid earth tide was included (magenta for L-band, green for C-band).

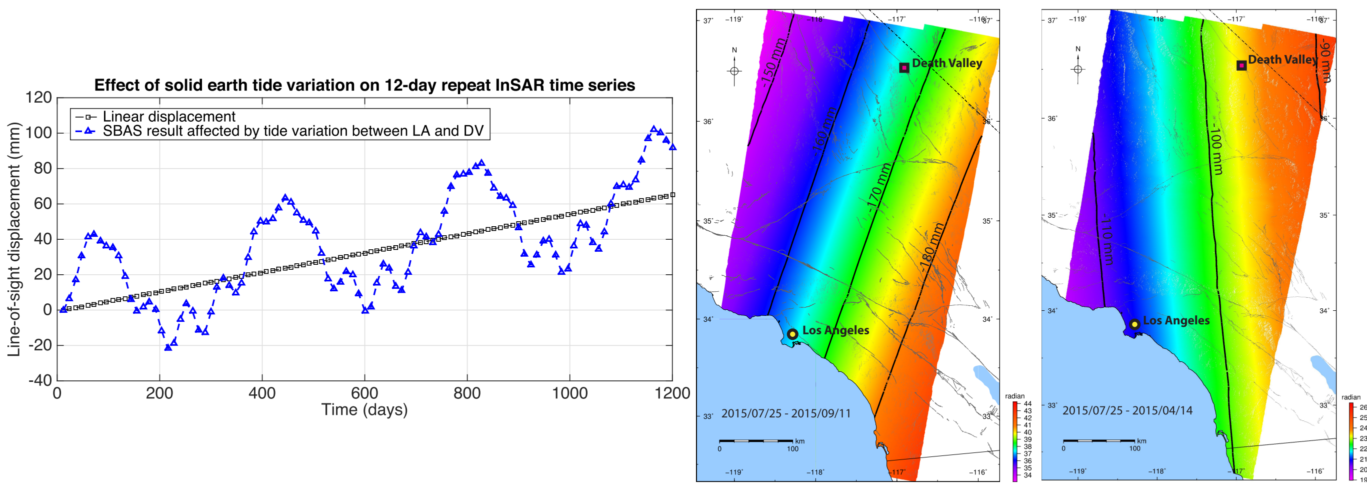

Fig. 3. (Left) SBAS time series from 3-year of InSAR acquisitions at 12-day sampling and a 60-day window for interferogram formation. This represents the difference in tidal displacement between Los Angeles and Death Valley (300 km) as a function of time. Black curve: assumed underlying linear trend. Blue curve: recovery when the solid earth tide is not corrected. (Middle and Right) Solid earth tide phase/displacement for two Sentinel-1 TOPS interferograms (July 25, 2015–September 11, 2015 and July 25, 2015–April 14, 2015).

The use of the phase closure constraint to solve for 2π integer ambiguities in unwrapped interferograms is common practice in InSAR time series analysis [16] [24], [25], [27]. The approach is to form all possible three-way loops in a set of interferograms so the problem can be written into the form of

$$\mathbf{G}m = d \tag{1}$$

$$\mathbf{G} = \begin{bmatrix} 1 & 1 & -1 & 0 & \cdots & 0 & 0 & 0 & 0 \\ 1 & 0 & 1 & -1 & \cdots & 0 & 0 & 0 & 0 \\ \vdots & \vdots & \vdots & \vdots & \vdots & \vdots & \vdots & \vdots & \vdots \\ 0 & 0 & 0 & 0 & \cdots & 1 & 1 & 0 & -1 \\ 0 & 0 & 0 & 0 & \cdots & 0 & 1 & 1 & -1 \end{bmatrix} \text{ and } d = \begin{bmatrix} 1 \\ 2 \\ \vdots \\ -1 \\ 0 \end{bmatrix} \tag{2}$$

where $\mathbf{G}$ is the matrix denoting the indices of interferograms to add or subtract to form the three-way loops and d is the vector of closure integers after summing interferograms over the loops, computing the median of each sum, and rounding to modulo of 2π. The unknown vector m is the integer ambiguity of each unwrapped interferogram. These can be subtracted from each interferogram to achieve global loop closure, and thus, provide an absolute phase connection between the first and last SAR image in the time series. One issue is that this inverse problem is not unique. To understand the nonuniqueness, consider a set of interferograms where the sums around all loops are zeros. Any solution m' that satisfies $\mathbf{G}m' = d$ can be added to or subtracted from m, without affecting the closure vector d. A trivial example is for a single triangular loop closing to 2π, the correction could be a 2π applied to one of the interferogram, or 2π s to all of them. To stabilize the problem, one has to apply regularization to the inverse problem.

Fattahi [26] used an L_2-norm minimization to find a solution for the problem. However, this least-squares approach may sometimes complicate the situation. For example, consider a single misclosure error of 4π in one triangular loop of interferograms. The L_2-norm will favor 2π corrections on two of the sides of the loop rather than a single 4π correction to one side. Here, we propose to use a lower norm penalty function that will result in fewer, but perhaps larger, ambiguity corrections. The ideal norm is the L_0-norm which corresponds to the compressed sensing/sparse recovery technique [28], and can be written as

$$\min \| m \|_0 \quad \text{s.t.} \| \mathbf{G}m - d \|_2 < \varepsilon \tag{3}$$

where the algorithm finds the minimum number of corrections required for global loop closure. After inversion, the nonzero

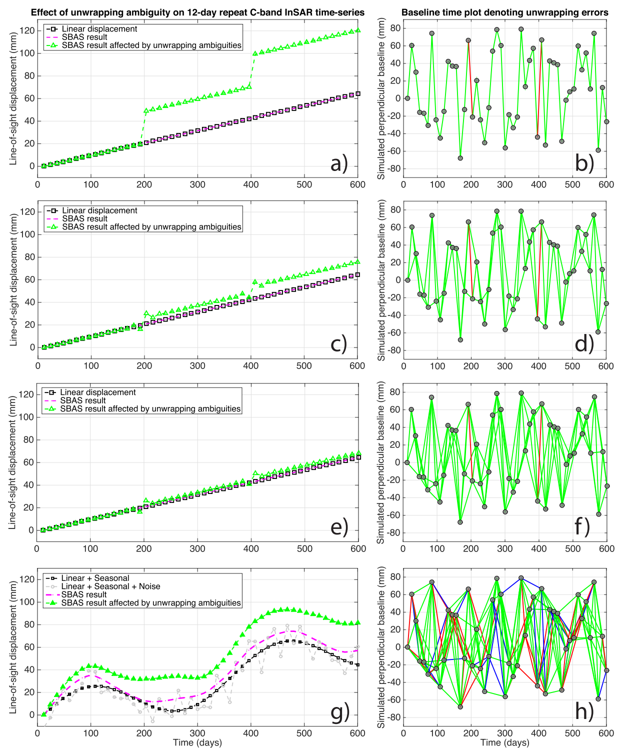

Fig. 4. Synthetic test of the phase unwrapping ambiguity on InSAR time-series. (b), (d), (f), and (h) Simulated baseline time plot for 50 SAR acquisitions with 12-day repeat. The interferometric pairs are selected using a 12-day (sequential), 24-day, 36-day, and 60-day temporal threshold for (b), (d), (f), and (h), respectively. Inside each plot, the green lines denote correctly unwrapped interferograms, the red lines denote an interferograms unwrapped with $+2\pi$ abiguity, and the blue lines denote interferograms with -2π ambiguity. (a), (c), and (e) corresponding time series where the black line denotes a prescribed linear deformation at 20 mm/yr, the magenta line denotes the SBAS solution using interferogram having no ambiguities, and the green line denotes the SBAS solution using the set of interferograms having two $+2\pi$ ambiguities. (g) More realistic case with a trend plus a seasonal signal and phase noise. There are unwrapping ambiguities of both sign on 30% of the interferograms. A simulation with no temporal smoothing of (g) is shown in Figure S4.

ms must be rounded to their nearest integer. However, the L_0-norm is nonconvex so it is hard to solve and unstable in the presence of noise [29]. Thus, we convexify the problem by following the approach in [30] and substitute the L_0-norm with the L_1-norm so the problem becomes

$$\min \| m \|_1 \quad \text{s.t.} \| \mathbf{G}m - d \|_2 < \varepsilon. \tag{4}$$

Again, after inversion, all the ms must be rounded to their nearest integer. A more practical approach is to introduce the Lagrange multiplier [31] to the problem setup so the minimization can be written as

$$\min(\| \mathbf{G}m - d \|_2 + \lambda \| m \|_1) \tag{5}$$

where λ can be chosen by analyzing the variance reduction of the inverse problem. In this case, where $\mathbf{G}$ and d are always integers, λ should be set as a very small number such as 0.01. If the initial inversion does not result in the closure of every loop, one can apply the partial correction and iterate until all loops close. Note that compared to GNSS ambiguity resolution correction, this algorithm is unable to determine the exact number of integer phase cycles, but rather it tries to bring all interferograms to the same unknown integer cycle, after which a deformation time-series can be correctly constructed. It is true that potentially there will still be a nonconstant m^* in the solution primarily due to other noise sources, such as atmospheric delay and solid earth tide. This is why we propose to apply the well-known corrections to the SLCs, such as the solid earth tide or ionospheric correction before solving for the ambiguities.

B. Performance Versus Number of Ambiguities

The percentage of interferograms having ambiguities will affect the accuracy of the inversion. This percentage will depend on the unmodeled errors in the interferograms as well as the InSAR correlation. Decorrelated interferograms commonly have phase unwrapping errors especially when the decorrelation disconnects regions of a well-correlated phase. We explore the adverse effects of ambiguities on SBAS time series recovery using the same signal characteristics as in Fig. 4(g) [i.e., trend + annual + noise in Fig. 5(a) gray curve]. The first case has 30% ambiguities of both signs. The recovered displacement time series (green) has a large drift error that is about 50 mm at the end of the time interval. The ambiguity-corrected time series (blue) matches the SBAS solution, where there are no ambiguities (magenta) except at the time of about 650 days when the inversion failed to recover all the ambiguities.

From our statistical tests, the performance curve [Fig. 5(b)] shows the methods works very well when the percentage of incorrectly unwrapped interferograms is low. Our experiences on 5 Sentinel-1 descending tracks in California (Fig. 6) shows the percentage of nonclosing loops [Fig. 5(b) (black curve)] is all below 40%, i.e., less than 20% of the interferograms have the $N2\pi$ shifts. All these cases fall at the left part of these curves in Fig. 5(b), where the performance of the algorithm is outstanding. The sparse assumption actually divided the problem setup into two subsets: when the number of ambiguities is low (left side, below 30%), the algorithm recovered the corrected loop closure was nearly zero [Fig. 6(b)]. When the number of ambiguities is high—above 40%, which is rare from our experience, the loop closure was gar from zero [Fig. 5(b)].

In addition to correcting the $N2\pi$ ambiguity of each interferogram, the approach also highlights integer phase unwrapping errors in areas that are decorrelated or have poor phase connections to the bulk of the interferogram. The remaining blocks that do not fully close at zero (e.g., area A in Fig. 6(a) and (b) can be recovered using the same algorithm or can be masked as unreliable. A pixel-wised correction is possible but not recommended since filtering generally destroys the closure criterion, which is the base of this recovery approach.

IV. Ionosphere Correction Can Cause an $N\pi$ Ambiguity

Recent advances in InSAR techniques allow scientists to correct ionospheric phase from interferograms using range split spectrum method [8], [10], [11], [13], where the low $\Delta\phi_L$ and high $\Delta\phi_H$ band-passed interferometric phase can be

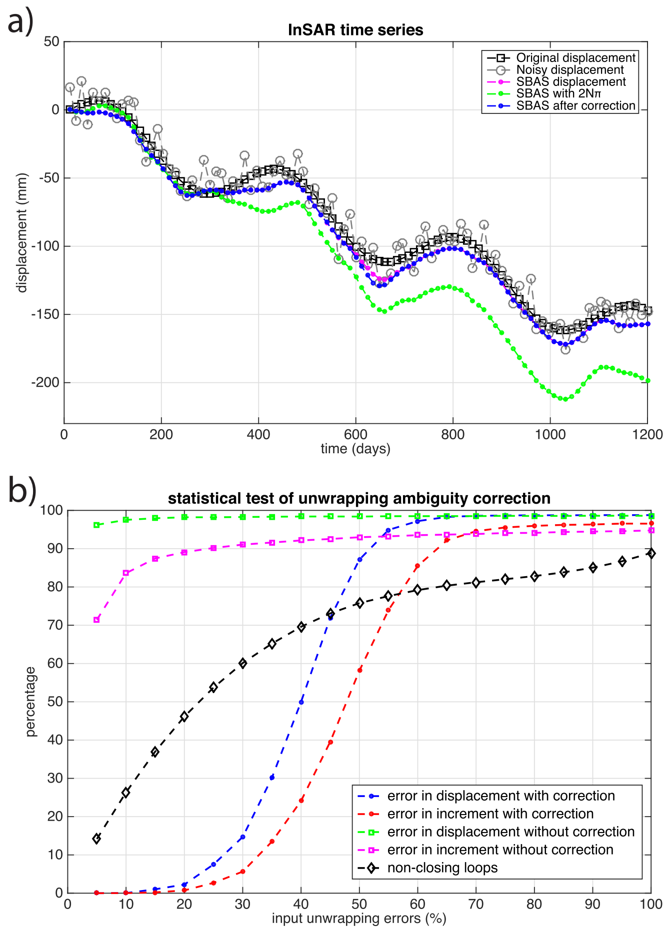

Fig. 5. Unwrapping ambiguity correction on InSAR time-series and the corresponding statistical tests on simulated data. (a) Black curve is a simulated InSAR time series consisting of a linear trend (50 mm/yr) plus seasonal (20-mm amplitude). The gray curve has atmospheric noise added (10-mm standard deviation). The magenta curve is the SBAS solution where atmospheric noise is included. The green curve is the SBAS solution when $\pm 2\pi$ or $\pm 4\pi$ ambiguities are added to 30% of the simulated interferograms. The blue curve is the SBAS solution after the ambiguities were corrected for using the above algorithm. For this extreme case of 30% ambiguities, the algorithm fails to solve for 7% of the ambiguities which causes the mismatch between the SBAS displacement with no ambiguities (magenta) and the ambiguity-corrected SBAS displacement. (b) Statistical test after running 20 000 simulations for different percentage of unwrapping errors for time series with different simulated atmospheric errors. Green and blue curves: percentage of mismatch in the displacement time-series before and after the correction, respectively. Magenta and red curves: percentage of mismatch in the solved increment of the time-series before and after the correction, respectively. Black curve: percentage of nonclosing triangular loops given certain percentage of added unwrapping ambiguities.

used to construct of dispersive component (ionosphere) $\Delta\phi_{\text{iono}}$ and non-dispersive (troposphere and deformation) component $\Delta\phi_{\text{non-disp}}$. The formulas are as in [10]

$$\Delta\phi_{\text{iono}} = \frac{f_H f_L}{f_0\left(f_H^2 - f_L^2\right)}(\Delta\phi_L f_H - \Delta\phi_H f_L) \tag{6}$$

$$\Delta\phi_{\text{non-disp}} = \frac{f_0}{\left(f_H^2 - f_L^2\right)}(\Delta\phi_H f_H - \Delta\phi_L f_L) \tag{7}$$

where f_0 is the carrier frequency, f_H is center frequency of the high band, and f_L is the center frequency of the low band. When performing this correction, localized unwrapping errors need to be identified and removed by examining the

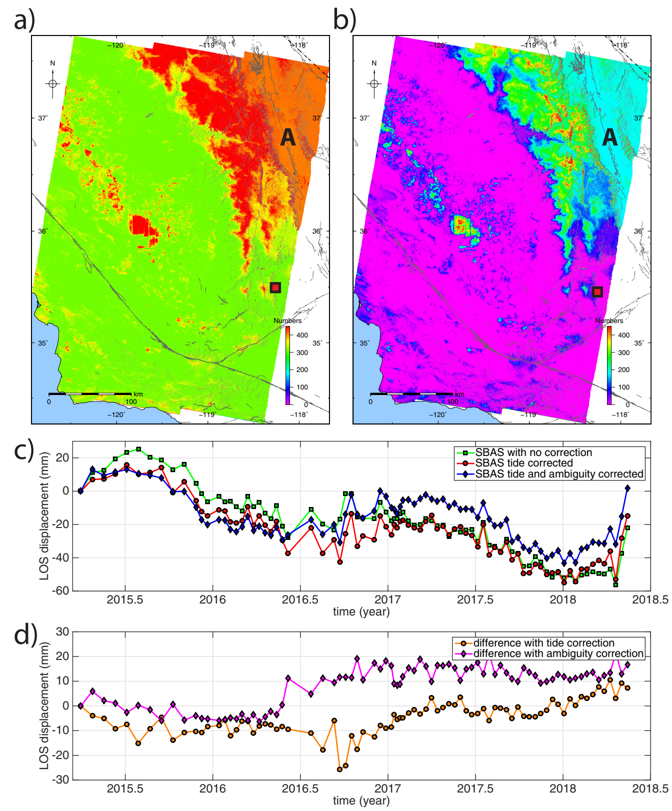

Fig. 6. (a) Number of nonclosing loops for each pixel before applying the unwrapping ambiguity correction for 81 Sentinel-1 scenes from track 144 (468 interferograms and 1207 loops). (b) Number of nonclosing loops after correction. (c) Line-of-sight displacement time series with and without corrections at the red square. (d) Differences caused to the time-series from the corrections at the red square.

unwrapped high and low interferograms. However, as discussed above, the absolute unwrapping ambiguity cannot be determined. There are two cases of absolute ambiguity errors. For case 1, the unwrapped phase of the high differs by $N2\pi$ from the unwrapped phase of the low. This causes an unreasonably large ionospheric phase that can be corrected by shifting either the high or low by $N2\pi$. For case 2 both the high and low have the same $N2\pi$ ambiguity. Similar to the common phase error discussed in [10] and [13], the resulting ionospheric correction $\Delta\phi_{\text{iono}}$ will be shifted by

$$\frac{N2\pi f_H f_L}{f_0(f_H + f_L)} = \frac{N2\pi(f_0 + \Delta f)(f_0 - \Delta f)}{f_0(2f_0)} = N\pi\left(1 - \frac{\Delta f^2}{f_0^2}\right) \tag{8}$$

which is roughly $N\pi$ since $\Delta f = (f_H - f_L)/2 \ll f_0$. When removing the ionospheric phase from the original interferogram, this term will contaminate the interferogram (Fig. 7), and thus, further affect the later InSAR time-series analysis. Below we discuss two approaches for correcting these $N\pi$ ambiguities in InSAR time series.

V. Ambiguity Correction/Time Series Algorithms

The current generation of SAR satellites has narrow bandwidths that are not well suited for ionospheric corrections.

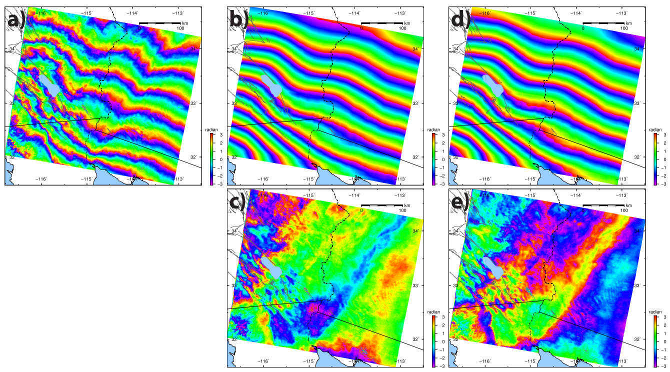

Fig. 7. Split-spectrum ionospheric correction applied to an ALOS-2 interferogram. (a) Original interferogram. (b) Ionospheric phase estimated using split-spectrum method. (c) Ionospheric phase corrected interferogram. (d) Estimated ionosphere correction if unwrapping ambiguity exists in both band-passed interferograms. (e) Applying the wrong correction from (d) to (a) results in a phase shift.

The high and low interferograms must be heavily filtered to suppress the noise even in well-correlated areas. Moreover, when the ionospheric correction is computed using (6), the denominator is very small which amplifies noise, as well as, localized unwrapping errors [10], [11], [13]. However, the planned NISAR mission will operate in two bands separated by ~60 MHz that will enable accurate ionospheric correction. Here, we propose two possible processing chains to address tide and ionospheric corrections, as well as, $N2\pi$ and $N\pi$ phase ambiguities. The first approach may be better suited to the case with a small bandwidth available for split-spectrum correction (e.g., ALOS-2) while the second may be better when a large bandwidth is available (e.g., NISAR).

Approach A—Low bandwidth (results in Figure S3)

1) Correct each SLC for the phase of the solid earth tide modulo 2π.
2) Unwrap interferograms and perform $N2\pi$ ambiguity correction for the stack.
3) Perform split spectrum ionospheric correction for each interferogram. Since these interferograms are close in frequency they will be similar to each other, as well as, the full-bandwith interferogram. Therefore, one can force the high and low interferograms to match the closest ambiguity of the full-bandwidth interferogram. However, because of nonuniqueness it is still possible that each interferogram could be shifted by $N\pi$.
4) Check for nonclosing loops.
5) Perform a second $N\pi$ ambiguity on the corrected stack if needed.

Approach B—High bandwidth

1) Correct each SLC for the phase of the solid earth tide modulo 2π.
2) Split the spectrum of the SLC's and construct stacks of high and low interferograms.
3) Perform $N2\pi$ ambiguity correction on each high and low stack individually.
4) Estimate and correct ionosphere for every full-bandwidth interferogram.
5) Unwrap the phase.
6) Perform a second $N\pi$ ambiguity on the corrected stack.

VI. Discussion and Conclusion

We demonstrate the adverse effects of phase ambiguities from solid earth tide and split-spectrum ionospheric correction on InSAR time-series. The 12-day repeat sampling of the current generation of InSAR satellites results in aliasing of the diurnal and semidiurnal tidal much longer periods. The absolute tide variations across an SAR scene will be wrapped so only the fractional part of the correction is important. This fractional tide will bias an L-band time series by up to 60 mm over 3 years while the effect is smaller at C-band (~10 mm). The relative tide variations across and along an unwrapped interferogram are typically 20–30 mm (same for C- and L-bands) due to the geographic variations in the tide but more importantly the change in look angle across the SAR swath. These tide errors map directly into the phase, and thus, have aliases of 64, 365.25, and 77 days caused by the 12-day exact repeat sampling of Sentinel-1 and NISAR. After the time series analysis, these relative tide errors can introduce large (+/− 20 mm) apparent deformation at a period of ~1 year that is easily confused with true seasonal deformation signals. The ocean loading tide will introduce a similar signal but over a shorter spatial scale [16]. There are studies that show that tide may also affect ranging accuracy [32], and thus, further affect SAR co-registration. Both the absolute and relative solid earth tide errors are easily corrected in the SLC, and we have implemented this correction in GMTSAR [33]. The ocean loading tidal correction can also be implemented, although it is less accurate. The standard split-spectrum ionospheric correction methods can also introduce ambiguities, but they are at half the rate of phase unwrapping ambiguities ($N\pi$ instead of the usual $N2\pi$). We have refined the standard loop-closure method to identify and correct for both types of ambiguities by solving for the minimum number (L_1-norm) of interferogram ambiguities that will result in loop closure. The algorithm performs well when the number of nonclosing loops is less than about 60%. A higher percentage of loop closures usually reflects decorrelated areas where the time series will be unreliable. The large bandwidth available for NISAR will facilitate the split-spectrum ionospheric correction, and we propose two algorithms to correct the ambiguities in InSAR time series, which will result in the absolute phase connection from the first to the last InSAR acquisitions.

Acknowledgment

The authors would like to thank ESA for the open policy on all the data sets and ASF and UNAVCO for archiving the data and orbital products. They would also like to thank JAXA for providing the ALOS-2 data. They would also like to thank D. Milbert for sharing his solid earth tide code on-line and M. Grant and S. Boyd for the convex optimization tool CVX.

References

[1] P. Prats-Iraola, R. Scheiber, L. Marotti, S. Wollstadt, and A. Reigber, "TOPS interferometry with TerraSAR-X," *IEEE Trans. Geosci. Remote Sens.*, vol. 50, no. 8, pp. 3179–3188, Aug. 2012.

[2] E. Sansosti, P. Berardino, M. Manunta, F. Serafino, and G. Fornaro, "Geometrical SAR image registration," *IEEE Trans. Geosci. Remote Sens.*, vol. 44, no. 10, pp. 2861–2870, Oct. 2006.

[3] R. Torres *et al.*, “GMES sentinel-1 mission,” *Remote Sens. Environ.*, vol. 120, pp. 9–24, May 2012.

[4] X. Xu, D. T. Sandwell, E. Tymofyeyeva, A. González-Ortega, and X. Tong, “Tectonic and anthropogenic deformation at the Cerro Prieto geothermal step-over revealed by sentinel-1A InSAR,” *IEEE Trans. Geosci. Remote Sens.*, vol. 55, no. 9, pp. 5284–5292, Sep. 2017.

[5] F. De Zan, M. Zonno, and P. López-Dekker, “Phase inconsistencies and multiple scattering in SAR interferometry,” *IEEE Trans. Geosci. Remote Sens.*, vol. 53, no. 12, pp. 6608–6616, Dec. 2015.

[6] P. Berardino, G. Fornaro, R. Lanari, and E. Sansosti, “A new algorithm for surface deformation monitoring based on small baseline differential SAR interferograms,” *IEEE Trans. Geosci. Remote Sens.*, vol. 40, no. 11, pp. 2375–2383, Nov. 2002.

[7] D. A. Schmidt and R. Bürgmann, “InSAR constraints on the source parameters of the 2001 Bhuj earthquake,” *Geophys. Res. Lett.*, vol. 33, no. 2, Jan. 2006, Art. no. L02315.

[8] F. Meyer, R. Bamler, N. Jakowski, and T. Fritz, “The potential of low-frequency SAR systems for mapping ionospheric TEC distributions,” *IEEE Geosci. Remote Sens. Lett.*, vol. 3, no. 4, pp. 560–564, Oct. 2006.

[9] E. Tymofyeyeva and Y. Fialko, “Mitigation of atmospheric phase delays in InSAR data, with application to the eastern California shear zone,” *J. Geophys. Res., Solid Earth*, vol. 120, no. 8, pp. 5952–5963, Aug. 2015.

[10] G. Gomba, A. Parizzi, F. De Zan, M. Eineder, and R. Bamler, “Toward operational compensation of ionospheric effects in SAR interferograms: The split-spectrum method,” *IEEE Trans. Geosci. Remote Sens.*, vol. 54, no. 3, pp. 1446–1461, Mar. 2016.

[11] H. Fattahi, M. Simons, and P. Agram, “InSAR time-series estimation of the ionospheric phase delay: An extension of the split range-spectrum technique,” *IEEE Trans. Geosci. Remote Sens.*, vol. 55, no. 10, pp. 5984–5996, Oct. 2017.

[12] C. Yu, Z. Li, N. T. Penna, and P. Crippa, “Generic atmospheric correction model for interferometric synthetic aperture radar observations,” *J. Geophys. Res., Solid Earth* vol. 123, no. 10, pp. 9202–9222, Oct. 2018.

[13] C. Liang, Z. Liu, E. J. Fielding, and R. Bürgmann, “InSAR time series analysis of L-Band wide-swath SAR data acquired by ALOS-2,” *IEEE Trans. Geosci. Remote Sens.*, vol. 56, no. 8, pp. 4492–4506, Aug. 2018.

[14] D. D. McCarthy and G. Petit, *IERS Conventions*. Berlin, Germany: IERS, 2004.

[15] D. C. Agnew, “NLOADF: A program for computing ocean-tide loading,” *J. Geophys. Res., Solid Earth*, vol. 102, no. B3, pp. 5109–5110, Mar. 1997.

[16] C. J. DiCaprio and M. Simons, “Importance of ocean tidal load corrections for differential InSAR,” *Geophys. Res. Lett.*, vol. 35, no. 22, Nov. 2008, Art. no. L22309.

[17] D. C. Agnew, “SPOTL: Some programs for ocean-tide loading,” Scripps Inst. Oceanogr., La Jolla, CA, USA, Tech. Rep., 2012. [Online]. Available: https://escholarship.org/uc/item/954322pg

[18] T. van Dam *et al.*, “Crustal displacements due to continental water loading,” *Geophys. Res. Lett.*, vol. 28, no. 4, pp. 651–654, Feb. 2001.

[19] Y. Fu, D. F. Argus, J. T. Freymueller, and M. B. Heflin, “Horizontal motion in elastic response to seasonal loading of rain water in the Amazon basin and monsoon water in southeast Asia observed by GPS and inferred from GRACE,” *Geophys. Res. Lett.*, vol. 40, no. 23, pp. 6048–6053, Dec. 2013.

[20] D. Kim and R. B. Langley, “GPS ambiguity resolution and validation: Methodologies, trends and issues,” in *Proc. 7th GNSS Workshop-Int. Symp. GPS/GNSS*, Seoul, South Korea, vol. 30, Nov. 2000, p. 12.

[21] W. Bertiger *et al.*, “Single receiver phase ambiguity resolution with GPS data,” *J. Geodesy*, vol. 84, no. 5, pp. 327–337, May 2010.

[22] H. A. Zebker, “User-friendly InSAR data products: Fast and simple timeseries processing,” *IEEE Geosci. Remote Sens. Lett.*, vol. 14, no. 11, pp. 2122–2126, Nov. 2017.

[23] W. Neely, A. Borsa, and F. Silverii, “GInSAR: A cGPS correction for enhanced InSAR time series,” *IEEE Trans. Geosci. Remote Sens.*, to be published.

[24] J. Biggs, T. Wright, Z. Lu, and B. Parsons, “Multi-interferogram method for measuring interseismic deformation: Denali fault, Alaska,” *Geophys. J. Int.*, vol. 170, no. 3, pp. 1165–1179, Sep. 2007.

[25] P. López-Quiroz, M.-P. Doin, F. Tupin, P. Briole, and J.-M. Nicolas, “Time series analysis of Mexico City subsidence constrained by radar interferometry,” *J. Appl. Geophys.*, vol. 69, no. 1, pp. 1–15, Sep. 2009.

[26] H. Fattahi, “Geodetic imaging of tectonic deformation with InSAR,” M.S. thesis, Univ. Miami, Coral Gables, FL, USA, 2015. [Online]. Available: https://search.proquest.com/docview/1718489348?pq-origsite=gscholar

[27] E. Hussain, A. Hooper, T. J. Wright, R. J. Walters, and D. P. S. Bekaert, “Interseismic strain accumulation across the central North Anatolian fault from iteratively unwrapped InSAR measurements,” *J. Geophys. Res., Solid Earth*, vol. 121, no. 12, pp. 9000–9019, Dec. 2016.

[28] D. L. Donoho, “Compressed sensing,” *IEEE Trans. Inf. Theory*, vol. 52, no. 4, pp. 1289–1306, Apr. 2006.

[29] R. G. Baraniuk, “Method and apparatus for distributed compressed sensing,” U.S. Patent 7,271747, Sep. 18, 2007.

[30] D. Malioutov, M. Cetin, and A. S. Willsky, “A sparse signal reconstruction perspective for source localization with sensor arrays,” *IEEE Trans. Signal Process.*, vol. 5, no. 8, pp. 3010–3022, Aug. 2005.

[31] H. Yao, P. Gerstoft, P. M. Shearer, and C. Mecklenbräuker, “Compressive sensing of the Tohoku-Oki Mw 9.0 earthquake: Frequency-dependent rupture modes,” *Geophys. Res. Lett.*, vol. 38, no. 20, Mar. 2011, Art. no. L20310.

[32] M. Eineder, C. Minet, P. Steigenberger, X. Cong, and T. Fritz, “Imaging geodesy—Toward centimeter-level ranging accuracy with TerraSAR-X,” *IEEE Trans. Geosci. Remote Sens.*, vol. 49, no. 2, pp. 661–671, Feb. 2010.

[33] D. T. Sandwell, X. Xu, R. Mellors, M. Wei, X. Tong, and P. Wessel. (2016). *GMTSAR: An InSAR Processing System Based on Generic Mapping Tools*. [Online]. Available: http://topex.ucsd.edu/gmtsar/tar/GMTSAR_2ND_TEX.pdf

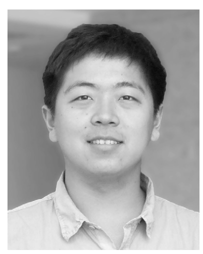

Xiaohua Xu received the B.S. degree in geophysics from the University of Science and Technology of China, Hefei, China, in 2012, and the Ph.D. degree in geophysics from the Scripps Institution of Oceanography, University of California at San Diego, La Jolla, CA, USA, in 2017.

He is currently a Post-Doctoral Researcher with Scripps Institution of Oceanography, where he is studying on InSAR technique and its application to geophysical problems. His research interests include developing InSAR processing techniques, studying crustal deformation related to interseismic tectonic processes and anthropogenic activities, imaging earthquake and volcanic sources, and monitoring reservoir depletion.

David T. Sandwell received the B.S. degree in physics from the University of Connecticut, Storrs, CT, USA, in 1975, and the Ph.D. degree in geophysics and space physics from the University of California at Los Angeles, Los Angeles, CA, USA, in 1981.

Since 1994, he has been a Professor of geophysics with the Scripps Institution of Oceanography, University of California at San Diego, La Jolla, CA, USA. His research interests include satellite geodesy crustal deformation and marine geophysics.

Prof. Sandwell is a member of the U.S. National Academy of Sciences and a fellow of the American Geophysical Union.